# A variable temperature neutron diffraction study of dual ion conducting $Sr_3V_2O_8$

Dylan N. Tawse [a], Sacha Fop [a,b], C. Ritter [c], Alfonso Martinez-Felipe [d], Abbie C. Mclaughlin [a,*]

[a] *Advanced Centre for Energy and Sustainability (ACES), The Chemistry Department, University of Aberdeen, Aberdeen, AB24 3UE, United Kingdom*
[b] *ISIS Facility, Rutherford Appleton Laboratory, Harwell, OX11 0QX, United Kingdom*
[c] *Institut Laue Langevin, 71 Avenue des Martyrs, BP 156, F-38042, Grenoble Cedex 9, France*
[d] *Chemical Processes and Materials Group, Just Transition Lab, School of Engineering, University of Aberdeen, King's College, Old Aberdeen, AB24 3UE, United Kingdom*

## ARTICLE INFO

## ABSTRACT

$Sr_3V_2O_8$ exhibits sizeable oxide ion and proton conductivity at 800 °C. In order to investigate any correlation between the crystal structure and electrical properties of $Sr_3V_2O_8$, a variable temperature neutron diffraction study has been performed. Results show that there is no change in crystal symmetry upon heating. However, the $VO_4$ tetrahedra are observed to become more distorted upon heating and more oblate in shape. The distortion arises due to a shortening of the apical V–O1 bond length and accompanying increase of the V–O2 bond length with temperature. Bond valence site energy analysis show that there is a reduction in the energy of the migration pathways for movement of the oxide ions as the Sr–V–Sr bottlenecks expand upon heating.

## 1. Introduction

Oxide ion and proton conductors find applications in numerous hydrogen-based energy devices such as electrolytes in ceramic fuel cells (solid oxide (SOFC) and proton ceramic (PCFC) fuel cells) as well as solid oxide electrolysers (SOEC) [1–5]. Currently, the greatest issue with these technologies is the high operating temperatures (>700 °C) required to allow the ionic species to diffuse through the electrolyte [2, 6,7]. It is therefore imperative that new materials are discovered which exhibit high oxide ion and/or proton conductivity at lower temperatures (400–600 °C) to act as intermediate temperature electrolytes in the next generation of ceramic fuel cells which will increase component lifespan and reduce start-up times. The ionic conductivity displayed by a material is strongly related to the crystal structure with the presence of structural disorder, oxygen vacancies and the arrangement of the cations being important features [4,8]. Ionic conduction has been reported for various crystal systems including cubic $ABO_3$ perovskite oxides such as sodium bismuth titanate (NBT) and doped lanthanum gallates (LSGM), hexagonal perovskite derivatives, $La_2Mo_2O_9$ (LAMOX) materials, brownmillerite structures (including $Ba_2In_2O_5$) and pyrochlores (including $Gd_2Ti_2O_7$) [9–19].

We have recently shown that several phases which crystallise with the hexagonal perovskite derivative structure can exhibit significant oxide ion and/or proton conductivity. For example, $Ba_3NbMoO_{8.5}$ exhibits a bulk oxide ionic conductivity of $2.2 \times 10^{-3}$ S cm$^{-1}$ at 600 °C [12]. $Ba_7Nb_4MoO_{20}$ displays bulk ionic conductivity of $3.16 \times 10^{-3}$ S cm$^{-1}$ in a dry environment at 600 °C [12,14]. However, when exposed to a humidified environment at 450 °C, the bulk ionic conductivity of $Ba_7Nb_4MoO_{20}$ increases to $3.55 \times 10^{-3}$ S cm$^{-1}$ confirming the presence of significant proton conduction [14].

The hexagonal perovskite derivatives described above are composed of perovskite and palmierite-like layers. The 9R perovskite is composed of $[AO_3]$ layers forming the $(hhc)_3$ stacking sequence. The palmierite structure displays the same $(hhc)_3$ stacking as the 9R perovskite. However, the palmierite structure is formed by oxygen-deficient $[AO_2]$ (c') layers resulting in isolated tetrahedral units separated by octahedral vacancies [20]. A disordered combination of the 9R perovskite and palmierite moieties are found in the palmierite-like (P-L) layers in both the $Ba_3M'M''O_{8.5}$ (M' = Nb/V, M" = Mo/W) family and $Ba_7Nb_4MoO_{20}$. It is within these P-L layers that ionic conduction pathways have been determined [15,21–23]. Other hexagonal perovskites such as $Ba_5Er_2Al_2ZrO_{13}$ which contain different structural features alongside tetrahedral units have also been found to exhibit significant oxide ion and/or proton conductivity [24]. $Ba_5Er_2Al_2ZrO_{13}$ is a 10H hexagonal perovskite formed of cubic $[BaO_3]$ layers (c) and oxygen deficient $[BaO]$ layers (h') displaying a stacking sequence of $(cch'cc)_2$. Two tetrahedral units are

---

* Corresponding author.
  *E-mail address:* a.c.mclaughlin@abdn.ac.uk (A.C. Mclaughlin).

connected *via* a shared apical oxygen on the h' layers resulting in the formation of an $Al_2O_7$ unit. These oxygen deficient h' layers are vital in the proton conduction mechanism for $Ba_5Er_2Al_2ZrO_{13}$ with proton sites present on the apical oxygen sites upon absorption of water onto the intrinsic oxygen vacancies. $Ba_5Er_2Al_2ZrO_{13}$ is a p-type electronic conductor under dry air but displays proton conductivity with a proton transport number $>0.99$ from 300 to 600 °C in humidified air. At 500 °C, $Ba_5Er_2Al_2ZrO_{13}$ exhibits a high proton conductivity of $3.0 \times 10^{-3} \, S \, cm^{-1}$ [24,25].

We recently investigated the electrical properties of the palmierites $A_3V_2O_8$ (A = Sr, Ba), to see if materials with pure palmierite layers could also exhibit ionic conductivity. $Sr_3V_2O_8$ was found to display substantial ionic conductivity with a bulk conductivity of $3.2 \times 10^{-5} \, S \, cm^{-1}$ in dry air and $1.0 \times 10^{-4} \, S \, cm^{-1}$ in humidified air at 600 °C showing the presence of both oxide ion and proton conduction [26]. The proton positions upon hydration were suggested through bond-valence site energy (BVSE) and density functional theory (DFT) calculations. Ionic conduction pathways were ascertained through BVSE and *ab initio* molecular dynamic simulations showing proton diffusion predominantly along the *ab* plane. Protons are present at the apical oxygen site (O1) and proton hopping arises across the O1 anions as well as from O1 to O2. Oxide ion diffusion pathways were simulated using *ab initio* molecular dynamics on models of $Sr_3V_2O_8$ with and without oxygen vacancies. When no oxygen vacancies were present, long-range diffusion and $VO_4$ rotational disorder was absent. However, upon introducing oxygen vacancies into the system both elements are present. Therefore, the oxide ion diffusion in $Sr_3V_2O_8$ was determined to be vacancy driven and arises when an oxygen atom shifts from a $VO_4$ tetrahedron to a vacant site present on an oxygen deficient $VO_3$ group through an intermediate $V_2O_7$ group [26].

In this study, we have performed a variable temperature neutron diffraction study of $Sr_3V_2O_8$ from 25 °C to 700 °C to investigate temperature related structural changes and their relationship to the electrical properties.

## 2. Experimental

$Sr_3V_2O_8$ was prepared by the solid-state synthesis of stoichiometric amounts of $SrCO_3$ ($\geq$99.9 %, Aldrich) and $V_2O_5$ (99.95 %, Aldrich). The starting materials were ground, pressed into a 13 mm pellet, and transferred to an alumina crucible to be heated at 1200 °C for 10 h before cooling to room temperature at 5 °C min$^{-1}$. The sample was reground, pelleted, and reheated until a phase pure product was obtained. Laboratory X-ray diffraction was performed using a PANalytical Empyrean diffractometer equipped with a Cu K$\alpha$ tube and Johansson monochromator to determine sample purity. Data were collected in the range $5 < 2\theta < 120°$ with a step size of 0.013°. For data collected at 700 °C, the sample was measured using an Anton Paar HTK 1200 N high temperature oven stage.

Variable temperature neutron diffraction data were collected at selected temperatures between 25 and 700 °C in air on the high-resolution diffractometer D2B at the Institut Laue-Langevin (ILL) in Grenoble, France. A 5 g sample was loaded into an open quartz tube and heated to the desired temperature and the data were recorded at $\lambda$ = 1.59432 Å for 2 h. Measurements were performed on the empty quartz tube at selected temperatures to allow for its contribution to the background to be subtracted from the sample data. The GSAS/EXPGUI package was used to perform Rietveld refinements on the obtained data [27,28].

Minimum bounding ellipsoid fitting was performed using the PIE-FACE software package to investigate the polyhedral distortion, $\sigma(R)$, and ellipsoidal shape, S, upon heating [29]. To quantify polyhedral distortion the standard deviation of the three primary ellipsoid radii, where $R_1 \geq R_2 \geq R_3$, was determined.

The programme *soft*BV was used to determine the bond valence sums (BVS) for the ions within the structure and perform bond-valence site
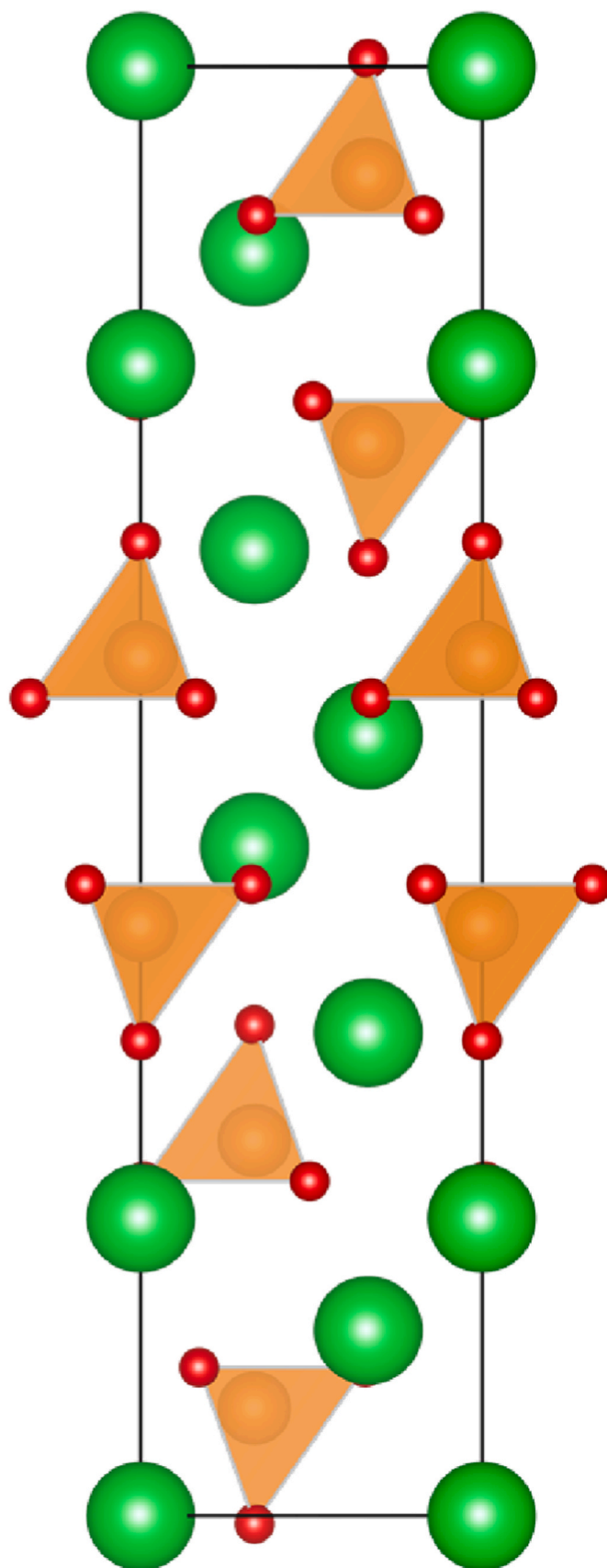


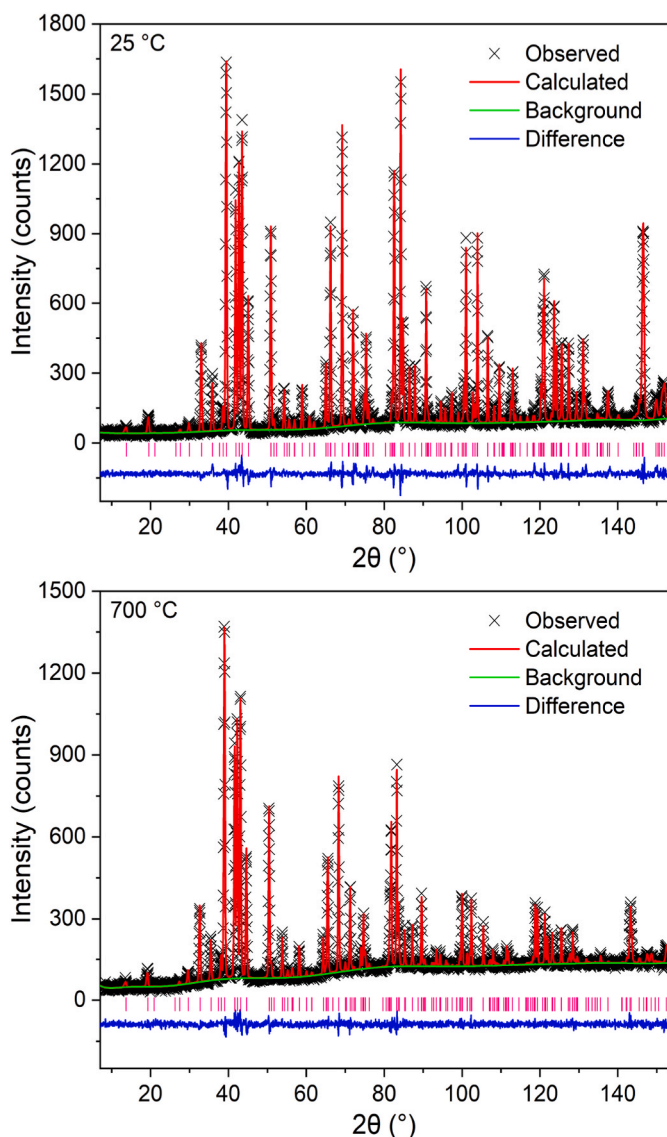**Fig. 1.** Crystal structure of $A_3B_2O_8$ which contains isolated $VO_4$ tetrahedra. Colours: green, Sr; orange, V; red, O.

**Fig. 2.** Rietveld refinement fit to the $R\bar{3}mH$ model of $Sr_3V_2O_8$ from neutron diffraction data recorded on the D2B instrument at the ILL at room temperature (top) and 700 °C (bottom). Black crosses show observed data, red line the Rietveld fit, green line is the background function, blue line the difference between the observed and calculated patterns, and vertical pink lines the reflection positions.

energy (BVSE) calculations on the structural models produced from Rietveld refinements [30,31]. BVSE landscapes for the interaction of a test $O^{2-}$ ion were calculated for the unit cell of the structural model which had been split into a dense grid with a resolution of 0.1 Å [30]. Regions of low BVSE could be determined through direct visualisation of the connectivity of the isosurfaces and by studying the calculated pathway segments which allowed diffusion pathways to be assigned. Relative energy barriers of the diffusion pathways could be extracted from the results of the BVSE model.

## 3. Results and discussion

The X-ray diffraction (XRD) pattern showed that $Sr_3V_2O_8$ was phase pure and could be indexed with the space group $R\bar{3}mH$ (Fig. S1). The crystal structure displays isolated tetrahedra separated by vacant octahedral units as shown in Fig. 1. Due to the low scattering cross section for neutrons displayed by vanadium, it was imperative to perform an initial
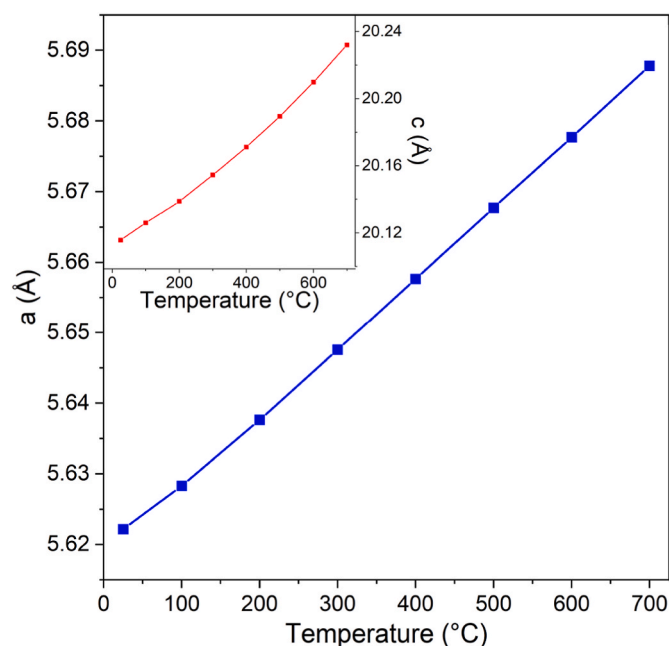


**Fig. 3.** Thermal variation of unit cell parameters $a$ and $c$ (inset). Both the $a$ and $c$ parameters show normal thermal expansion upon increasing the temperature.

Rietveld refinement using X-ray diffraction data to determine the fractional occupancies of V. The Sr atoms occupy two Wyckoff sites with Sr1 present on the $3a$ site and Sr2 on the $6c$ site. V can be found on the $6c$ position while the oxygen atoms are found on two positions: O1 on the $6c$ site and O2 on the $18h$ site. The V fractional occupancy was allowed to refine freely in the XRD refinement and refined to within ±1 % of the full occupancy, and hence was subsequently fixed at 1.0. The refinement displayed a good match between the calculated and observed histograms and the following statistical parameters were obtained: $\chi^2 = 4.56$, $R_p = 4.85$ %, $R_{wp} = 6.82$ % (Fig. S2 and Table S1). X-ray diffraction data were also recorded at 700 °C and the Rietveld refinement and refined atomic parameters are shown in Fig. 3 and Table S2 respectively. The results show there is no change in crystal symmetry upon heating and the V site
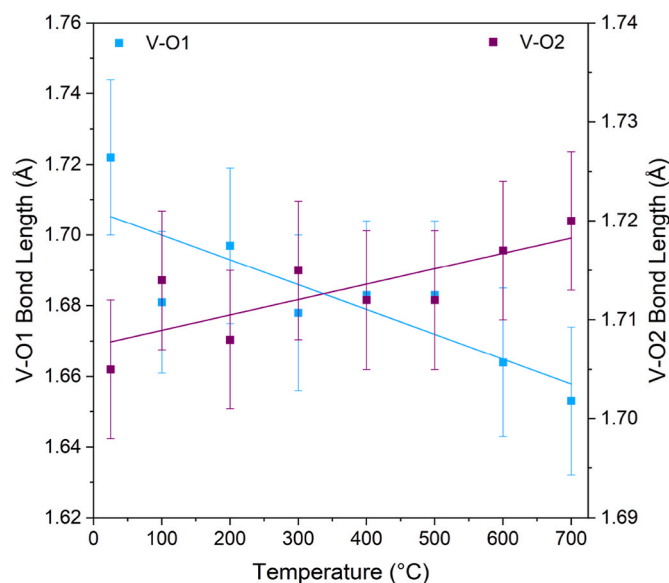


**Fig. 4.** Thermal variation of V–O1 (blue) and V–O2 (purple) bond lengths. The V–O1 bond length decreases while the V–O2 bond length increases as the temperature rises.

remains fully occupied.

The previously reported palmierite structure obtained from Rietveld refinement with High-Resolution Powder Diffractometer (HRPD) data on the HRPD instrument at ISIS (Rutherford Appleton Laboratory, Harwell, Oxford, UK) was used as a starting model for the variable temperature neutron refinements [26]. The atomic displacement parameters were modelled anisotropically for all atoms except V over the whole temperature range. When allowed to refine either isotropically or anisotropically, the atomic displacement parameters for V were unrealistic and were therefore set to $U_{iso} = 0.00127$ Å$^2$ as obtained from the initial refinement from the HRPD data. All Sr and O fractional occupancies refined to within $\pm 1$ % of the full occupancy at all temperatures and were subsequently fixed at 1.0 with V atoms fixed to 1.0 as previously determined from the XRD refinement results.

An excellent Rietveld refinement fit to the $R\,\overline{3}\,mH$ model is observed at all temperatures from 25 °C to 700 °C, as shown in Fig. 2, so that there is no change in crystal symmetry upon heating. The statistical parameters at 25 °C and 700 °C are respectively $\chi^2 = 3.81$, $R_p = 4.91$ %, $R_{wp} = 5.33$ % and $\chi^2 = 2.27$, $R_p = 4.09$ %, $R_{wp} = 4.29$ %. The Rietveld fits for 400 °C and 600 °C are shown in Fig. S4. The results from the Rietveld refinement are displayed in Table S3.

The thermal variation of the unit cell parameters is displayed in Fig. 3 and regular thermal expansion of both the $a$ and $c$ parameters is observed from 25 °C to 700 °C. Upon increasing the temperature, the V–O1 bond length decreases alongside an accompanying increase in the V–O2 bond length (Fig. 4 and Table S4). All Sr–O bonds were found to show a small increase in length upon heating from 25 °C to 700 °C. As the temperature increases subtle changes are observed for the O1–V–O2 and O2–V–O2 angles. The O1–V–O2 angle increases from 108.6(7) ° to 110.0(7) ° and the O2–V–O2 angle decreases from 110.3(7) ° to 108.9(7) ° at 25 °C and 700 °C respectively.

The variation of the unit cell parameters and bond lengths with temperature show no anomalies upon heating so that no structural rearrangement is observed for Sr$_3$V$_2$O$_8$ from 25 °C to 700 °C. This is in contrast with other hexagonal perovskite derivatives that contain P-L layers such as Ba$_3$NbMoO$_{8.5}$ and Ba$_7$Nb$_4$MoO$_{20}$ [12,14]. A structural rearrangement has been reported for Ba$_3$NbMoO$_{8.5}$ above 300 °C which involves an increase in the ratio of tetrahedral: octahedral Nb/MoO$_x$ units [12]. Ba$_7$Nb$_4$MoO$_{20}$ displays a similar structural rearrangement above 300 °C in which there is an increase in lower coordination environments as a result of the change in the fractional occupancies of the corresponding O crystallographic sites [14]. The structural rearrangements arise due to the ability of these materials to absorb a considerable amount of water which causes a redistribution of metal cations from the M1 site on the P-L layers to the vacant octahedral M2 site upon hydration. DFT calculations have suggested that the presence of a proton in a position between the M1 and O1/O2 sites forces this movement of the M1 cation onto the M2 site. Upon heating, the cations move back to the M1 site as a result of water loss from the P-L layers which further corroborates that it is the presence of water that induces the structural rearrangements for Ba$_3$NbMoO$_{8.5}$ and Ba$_7$Nb$_4$MoO$_{20}$ [14,23].

We recently reported that the proton concentration for Sr$_3$V$_2$O$_8$ is considerably lower than both Ba$_3$NbMoO$_{8.5}$ and Ba$_7$Nb$_4$MoO$_{20}$, with Sr$_3$V$_2$O$_8$ displaying a water concentration of 0.024 molecules of H$_2$O per formula unit compared to 0.80 and 0.20 for Ba$_3$NbMoO$_{8.5}$ and Ba$_7$Nb$_4$MoO$_{20}$, respectively [26]. These higher levels of hydration occur as the cation sublattice of Ba$_3$NbMoO$_{8.5}$ and Ba$_7$Nb$_4$MoO$_{20}$ both show high flexibility regarding the movement of cations from the M1 to M2 site allowing these structures to accommodate for higher levels of water uptake [14,23,26]. We recently performed a variable temperature neutron diffraction study on Ba$_3$VWO$_{8.5}$ in which only subtle changes to the O2/O3 fractional occupancies were witnessed from 30 to 800 °C and therefore no structural rearrangement occurs. TGA-MS data showed no significant water loss from 25 to 1000 °C indicating the uptake of water by Ba$_3$VWO$_{8.5}$ is very small. It was concluded that the ordering of the
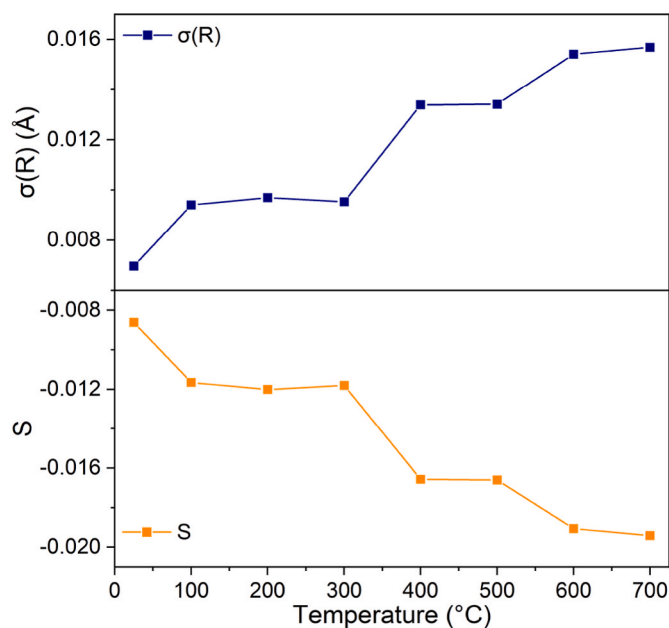


**Fig. 5.** Thermal variation of polyhedral distortion (navy) and the ellipsoidal shape parameter (orange) of VO$_4$ tetrahedra. Polyhedral distortion increases alongside a decrease in the ellipsoidal shape parameter upon heating.

metal cations onto the M1 site, due to the preference of V$^{5+}$ to adopt a tetrahedral geometry, inhibits the uptake of water by Ba$_3$VWO$_{8.5}$ [32]. Hence, the absence of a structural rearrangement for Sr$_3$V$_2$O$_8$ most likely also results from the significantly lower proton concentration.

The PIEFACE software package was used to analyse the minimum bounding ellipsoid at each temperature. The minimum bounding ellipsoid of interest can be described as the ellipsoid of the smallest volume which contains all the atoms of the VO$_4$ tetrahedral units [29]. Minimum bounding ellipsoid analysis allows for facile determination of polyhedral distortion $\sigma(R)$ and the ellipsoidal shape parameter (S). $\sigma(R)$ is described as the standard deviation of the three principal ellipsoid radii ($R_x$, $R_y$ and $R_z$). S has a range of $-1 \leq S \leq 1$, where a sphere is represented by $S = 0$, while $S < 0$ indicates an oblate ellipsoid and $S > 0$ a prolate ellipsoid.

The polyhedral distortion for Sr$_3$V$_2$O$_8$ increases as the temperature rises (Fig. 5, top), with $\sigma(R)$ increasing from $6.963 \times 10^{-3}$ Å at 25 °C to $1.569 \times 10^{-2}$ Å at 700 °C. Hence, the VO$_4$ units become more distorted as the temperature rises. The ellipsoidal shape parameter decreases with an increase in temperature (Fig. 5, bottom) from $-0.00862$ at 25 °C to $-0.0194$ at 700 °C. Therefore, axial compression of the polyhedra is observed, so that the VO$_4$ units become more oblate. These changes to the VO$_4$ units are observed alongside the changes in the V–O1 and V–O2 bond lengths. The O1 $z$ position decreases upon heating which leads to shortening of the apical V–O1 bond length. The O2 $x$ position decreases alongside an increase in the O2 $y$ position from 25 °C to 700 °C causing the V–O2 bond length to increase. These changes to the positions of the oxygen atoms cause the tetrahedral units to become increasingly distorted as temperature rises. No trends are observed for the vanadium $z$ position or the out-of-centre displacement (D) therefore these factors are

**Table 1**
Calculated bond valence sums from the neutron diffraction bond lengths at 25 °C and 700 °C.

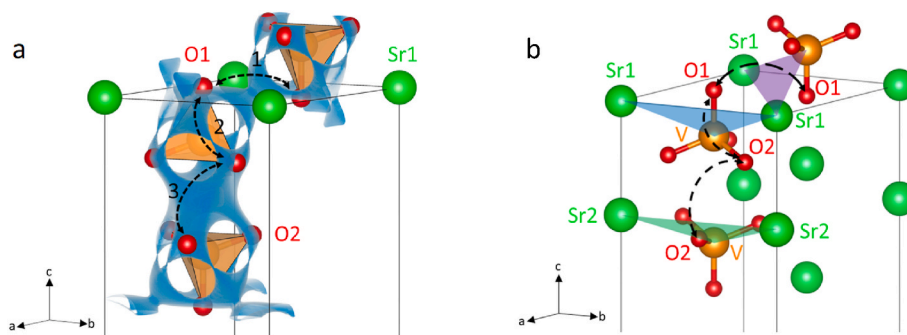| Atom | Bond valence sum (25 °C) | Bond valence sum (700 °C) |
|------|--------------------------|----------------------------|
| **Sr1** | 1.79 | 1.69 |
| **Sr2** | 1.93 | 1.77 |
| **V1** | 5.01 | 5.05 |
| **O1** | −1.82 | −1.94 |
| **O2** | −2.00 | −1.91 |

**Fig. 6.** (a) BVSE map for a test $O^{2-}$ ion in $Sr_3V_2O_8$ showing exchange between O1–O1 (1), O1–O2 (2) and O2–O2 (3) positions. Isosurface levels are drawn at < 0.65 eV. (b) Part of the refined structure of $Sr_3V_2O_8$ showing the Sr–V–Sr bottlenecks for O1–O1, O1–O2 and O2–O2 oxide ion migration respectively.

independent of temperature. Hence, the tetrahedral distortion is exclusively related to the positions of the O1 and O2 ions rather than changes in the position of the vanadium atom. The thermal variation of the distortion of the $VO_4$ tetrahedra in $Sr_3V_2O_8$ is hence different to the distortion of the $(Nb/Mo)O_x$ polyhedra reported in $Ba_3NbMoO_{8.5}$, where a change in the polyhedral distortion with temperature is driven by the second order Jahn-Teller effect [33]. The bond valence sums [34] for the different atoms within the $Sr_3V_2O_8$ structure are shown in Table 1. At 25 °C Sr1 and O1 are both underbonded. The results show that the subtle distortion of the $VO_4$ tetrahedra at 700 °C relieves the underbonding at the O1 site. However both Sr1 and Sr2 become more underbonded as the O1 and O2 atoms move away from the Sr1 and Sr2 site upon heating.

Bond valence site energy (BVSE) calculations show three dimensional connectivity across the different oxygen positions as previously reported (Fig. 6(a)) [26]. The relative energy barriers at 25 °C and 700 °C are respectively 0.238 eV and 0.216 eV for O1–O1 hopping; 0.328 eV and 0.246 eV for O1–O2 hopping and 0.628 eV and 0.426 eV for O2–O2 hopping. The results suggest that the BVSE barriers for oxide ion migration from O1–O2 and O2–O2 are reduced upon heating to 700 °C. The Sr–V–Sr triangular bottlenecks for oxide ion migration are shown in Fig. 6(b). A potential reason for the reduced energy barriers would hence be a result of an increase in size of the Sr–V–Sr bottlenecks because of the thermal expansion of the unit cell upon heating.

## 4. Conclusions

A variable temperature neutron diffraction study has been performed on the dual ion conducting hexagonal perovskite derivative $Sr_3V_2O_8$. The $R\overline{3}mH$ space group is observed at all temperatures and the $VO_4$ tetrahedra become more distorted upon heating from 25 °C to 700 °C. Structural rearrangements have been previously reported for the hexagonal perovskite derivatives $Ba_3NbMoO_{8.5}$ and $Ba_7Nb_4MoO_{20}$ upon dehydration above 300 °C. The hydration of $Sr_3V_2O_8$ is significantly lower than reported for $Ba_3NbMoO_{8.5}$ and $Ba_7Nb_4MoO_{20}$ so that there is no evidence of a structural rearrangement upon heating. BVSE calculations have been performed and the results suggest that the energy barriers for movement of the oxide ions from O1 to O2 and O2 to O2 are reduced due to an increase in the size of the Sr–V–Sr bottlenecks with thermal expansion of the unit cell. This could result in enhanced oxide ion conductivity with temperature, and a potential route to increase the oxide ionic conductivity in $Sr_3V_2O_8$ further could be to add chemical dopants that are known to expand bottlenecks such as $Cs^+$ and $Bi^{3+}$ [35].

## CRediT authorship contribution statement

**Dylan N. Tawse:** Data curation, Formal analysis, Investigation, Methodology, Visualization, Writing – original draft, Writing – review & editing. **Sacha Fop:** Data curation, Formal analysis, Investigation, Visualization, Writing – original draft, Writing – review & editing. **C. Ritter:** Data curation, Formal analysis, Writing – original draft, Writing – review & editing. **Alfonso Martinez-Felipe:** Formal analysis, Supervision, Visualization. **Abbie C. Mclaughlin:** Conceptualization, Formal analysis, Investigation, Project administration, Resources, Supervision, Validation, Visualization, Writing – original draft, Writing – review & editing.

## Declaration of competing interest

The authors declare that they have no known competing financial interests or personal relationships that could have appeared to influence the work reported in this paper.

## Data availability

Data will be made available on request.

## Appendix A. Supplementary data

Supplementary data to this article can be found online at https://doi.org/10.1016/j.jssc.2023.124512.

## References

[1] J.H. Shim, Nat. Energy 3 (2018) 168–169.
[2] C. Duan, J. Tong, M. Shang, S. Nikodemski, M. Sanders, S. Ricote, A. Almansoori, R. O'Hayre, Science 349 (2015) 1321–1326.
[3] A.J. Jacobson, Chem. Mater. 22 (2010) 660–674.
[4] L. Malavasi, C.A.J. Fisher, M.S. Islam, Chem. Soc. Rev. 39 (2010) 4370–4387.
[5] M.A. Laguna-Bercero, J. Power Sources 203 (2012) 4–16.
[6] T.A. Adams, J. Nease, D. Tucker, P.I. Barton, Ind. Eng. Chem. Res. 52 (2013) 3089–3111.
[7] B.C.H. Steele, A. Heinzel, Nature 414 (2001) 345–352.
[8] S. Fop, K.S. McCombie, E.J. Wildman, J.M.S. Skakle, A.C. Mclaughlin, Chem. Comm. 55 (2019) 2127–2137.
[9] M. Li, M.J. Pietrowski, R.A. De Souza, H. Zhang, I.M. Reaney, S.N. Cook, J. A. Kilner, D.C. Sinclair, Nat. Mater. 13 (2014) 31–35.
[10] F. Yang, M. Li, L. Li, P. Wu, E. Pradal-Velázquez, D.C. Sinclair, J. Mater. Chem. A 5 (2017) 21658–21662.
[11] P. Majewski, M. Rozumek, F. Aldinger, J. Alloys Compd. 329 (2001) 253–258.
[12] S. Fop, J.M.S. Skakle, A.C. McLaughlin, P.A. Connor, J.T.S. Irvine, R.I. Smith, E. J. Wildman, J. Am. Chem. Soc. 138 (2016) 16764–16769.
[13] K.S. McCombie, E.J. Wildman, S. Fop, R.I. Smith, J.M.S. Skakle, A.C. McLaughlin, J. Mater. Chem. A 6 (2018) 5290–5295.
[14] S. Fop, K.S. Mccombie, E.J. Wildman, J.M.S. Skakle, J.T.S. Irvine, P.A. Connor, C. Savaniu, C. Ritter, A.C. Mclaughlin, Nat. Mater. 19 (2020) 752–757.

[15] A. Gilane, S. Fop, F. Sher, R. Smith, A. Mclaughlin, J. Mater. Chem. A 8 (2020) 16506–16514.
[16] F. Goutenoire, O. Isnard, R. Retoux, P. Lacorre, Chem. Mater. 12 (2000) 2575–2580.
[17] J.B. Goodenough, J.E. Ruiz-Diaz, Y.S. Zhen, Solid State Ionics 44 (1990) 21–31.
[18] G.B. Zhang, D.M. Smyth, Solid State Ionics 82 (1995) 153–160.
[19] S.A. Kramer, H.L. Tuller, Solid State Ionics 2738 (1995) 15–23.
[20] J. Darriet, M.A. Subramanian, J. Mater. Chem. 5 (1995) 543–552.
[21] S. Fop, K. McCombie, R.I. Smith, A.C. McLaughlin, Chem. Mater. 32 (2020) 4724–4733.
[22] D.N. Tawse, A. Gilane, S. Fop, A. Martinez-Felipe, F. Sher, R.I. Smith, A. C. Mclaughlin, Inorg. Chem. 60 (2021) 13550–13556.
[23] S. Fop, J.A. Dawson, A.D. Fortes, C. Ritter, A.C. McLaughlin, Chem. Mater. 33 (2021) 4651–4660.
[24] T. Murakami, J.R. Hester, M. Yashima, J. Am. Chem. Soc. 142 (2020) 11653–11657.
[25] S. Fop, J. Mater. Chem. A 9 (2021) 18836–18856.

[26] S. Fop, J.A. Dawson, D.N. Tawse, M.G. Skellern, J.M.S. Skakle, A.C. McLaughlin, Chem. Mater. 34 (2022) 8190–8197.
[27] A.C. Larson, R.B. Von Dreele, General Structure Analysis System (GSAS), Report LAUR, Los Alamos National Laboratory, 1994.
[28] B.H. Toby, J. Appl. Crystallogr. 34 (2001) 210–213.
[29] J. Cumby, J.P. Attfield, Nat. Commun. 8 (2017) 1–8.
[30] H. Chen, L.L. Wong, S. Adams, Acta Crystallogr. B Struct. Sci. Cryst. Eng. Mater. 75 (2019) 18–33.
[31] H. Chen, S. Adams, IUCrJ 4 (2017) 614–625.
[32] A. Gilane, S. Fop, D.N. Tawse, C. Ritter, A.C. McLaughlin, Inorg. Chem. 61 (2022) 1597–1602.
[33] S. Fop, E.J. Wildman, J.T.S. Irvine, P.A. Connor, J.M.S. Skakle, C. Ritter, A. C. McLaughlin, Chem. Mater. 29 (2017) 4146–4152.
[34] I.D. Brown, R.D. Shannon, Acta Crystallogr. 29 (1973) 266–282.
[35] W. Zhang, K. Fujii, E. Niwa, M. Hagihala, T. Kamiyama, M. Yashima, Nat. Commun. 11 (2020) 1–8.